A redox-active perylene-anthraquinone donor-acceptor conjugated microporous polymer with an unusual electron delocalization channel for photocatalytic reduction of uranium (VI) in strongly acidic solution

Fengtao Yu [1], Zhiqiang Zhu [1], Chuangye Li, Wanru Li, Renping Liang, Shanshan Yu, Zhenzhen Xu, Fangru Song, Qiang Ren, Zhibin Zhang [*]

State Key Laboratory of Nuclear Resources and Environment, School of Chemistry, Biology and Materials Science, East China University of Technology, Nanchang 330013, PR China

ARTICLE INFO

ABSTRACT

Achieving photoreduction uranium with D-A type conjugated microporous polymers in strongly acidic radio-active wastewater holds great promise but is extremely challenging, as it requires proper electron transport channels. Herein, a redox-active perylene-anthraquinone D−A conjugated microporous polymer photocatalyst (**ECUT-AQ**) which electron-rich perylene unit as donor and electron-deficient anthraquinone (AQ) as acceptor is innovatively reported. The results clearly demonstrates that AQ with dual characteristics of electron deficiency and redox activity plays a key role in photocatalytic reduction of UO_2^{2+} to UO_2. On one hand, the constructed D-A structure induces the formation of a huge built-in electric field, which enhances the intramolecular charge transfer, thus significantly broadening visible light absorption range and improving electron-hole pairs separation efficiency. On the other hand, and very significantly, the redox-active AQ acts as a matched electron transfer channel, which further accelerates the photogenerated electrons transfer from the photocatalyst to the UO_2^{2+}. Consequently, the **ECUT-AQ** achieves 86% photoreduction UO_2^{2+} removal within two hours irradiation and obtains an impressive reduction rate constant ($k = 0.015$ min^{-1}, pH=1 and $T = 293.15$ K). Encouragingly, the current work can enlighten a whole new direction for the subsequent cultivation of more practical metal-free photocatalysts for purification radioactive wastewater.

1. Introduction

Nuclear energy, the clean energy with the most potential for sustainable development of mankind, is indispensable for achieving the new development concept of "carbon peak and carbon neutrality"[1,2]. Paradoxically, the continuous perfection of the nuclear power industry chain will inevitably discharge a large amount of uranium-containing wastewater, which is an extremely terrible environmental radioactive pollutant [3–5]. Up to now, several conventional methods such as adsorption [6], ionic exchange [7], co-precipitation [8], solvent extraction [9], and evaporation [10] have been proposed to eliminate uranium (abbreviated as U(VI)) before the wastes can be finally disposed in geological repositories. Although some of these strategies have made encouraging progress, serious technical shortcomings have greatly restricted their practical applications. For instance, the selective

adsorption efficiency of U(VI) is inhibited by harsh environment of waste water such as high salinity or acidity and strong radioactivity. Therefore, it is urgent to search after more efficient approach to removal of uranium pollutants from nuclear industry wastewater.

Recently, the emerging green removing uranium technologies via semiconductor photocatalytic reduction the highly mobile U(VI) to sparingly soluble U(IV) have attracted considerable interdisciplinary attention [11–16]. Among the various types of photocatalysts that have been reported, metal-free conjugated microporous polymers (CMPs), featured by their highly flexible design, wide visible-light absorption, diverse building blocks and tunable electronic structure [17–22], have been considered as a promising photocatalysts that perfectly complements metal-containing inorganic semiconductors [23–27] for uranium reduction. Among them, the donor-acceptor (D-A) type CMPs exhibit relatively satisfactory photocatalytic activity because D and A have

---

significantly different electron affinity, which then induce a large dipole moment, thereby forming a stronger built-in electric field [28–30]. For example, our group has synthesized a series of perylene-based D-A CMPs for the first time, and explored the effect of acceptor modulation on the photoreduction uranium activity [31]. Coincidentally, we have synthesized a series of D-A-A conjugated polymers with statistical copolymerization, which further improved the activity of photocatalytic reduction of uranium [32]. Although promising progress has been made, our stamina to deal with nuclear wastewater is still insufficient. The bottleneck lies in nuclear industry wastewater is highly acidic (pH≤2), and the current photocatalysts basically inactive under such harsh conditions [33–39], which is predominantly attributed to the competition of proton with uranyl ion for photo-generated electrons and adsorption/catalytic sites. From this perspective, it is imperative to hunt visible-light-driven organic polymer photocatalyst with unprecedented electron-hole separation efficiency to achieve the excellent photocatalytic uranium reduction activity under strong acid conditions.

Interestingly, anthraquinone (marked as AQ) possesses the dual characteristics of redox activity and strong electron deficiency, thus it is a promising block for constructing efficient D-A-type CMP photocatalysts to realize the reduction of uranium under strongly acidic conditions. For redox activity, similar to plastoquinone in the natural photosynthetic system, is a two-electron, two-proton transporter (as shown in Fig.S3): it can be rapidly reduced to oxanthranol (OAO) under strongly acidic conditions by the electrons, then the OAO quickly oxidized to AQ by the holes [40,41]. Apparently, the unique redox properties of AQ prompt it to act as an electron transfer bridge, providing an efficient pathway for electron transfer during photocatalytic reactions. Furthermore, the electron-deficient AQ unit has been widely selected as the candidate for the electron-acceptor of D-A conjugated polymers which is conducive to the generation of the built-in electric field and promotes the separation of excitons [42,43]. For example, Liu's group has successfully synthesized anthraquinone-based conjugated polymers (DA-CMPs) via oxidative coupling reactions for efficient photocatalytic organic synthesis [44]. Hereafter, Kim and coworkers innovatively describe the exploitation of the selective catalytic property of AQ for solar photocatalytic synthesis of hydrogen peroxide (H$_2$O$_2$) as a green and energy-intensive industry-benchmark processes

that also rely on AQ catalysis [45].

Herein, as shown in Scheme 1, a redox-active D-A conjugated microporous polymer (named as **ECUT-AQ**), in which perylene as the donor and AQ unit as the acceptor, has been creatively synthesized for achieving efficient and highly selective photoreduction of uranium in strongly acidic aqueous solution (pH=1). To verify that the introduction of AQ unit can significantly improve photocatalytic uranium reduction activity, the reference polymer containing anthracene unit (marked as **ECUT-AC**) has been synthesized correspondingly. As expected, the experimental results combined with the theoretical calculation results show that introduction of AQ: (i) broadens visible light response range; (ii) promotes electron-hole pairs separation and accelerates photogenerated charge transfer; (iii) improves the selectivity adsorption to uranyl ions under strong acid conditions, thereby significantly enhancing photoreduction uranium activity. It is strikingly that **ECUT-AQ** achieves 86% uranium removal rate in a pH= 1 aqueous solution containing 50 ppm UO$_2^{2+}$ after irradiation for 2 h. To the best of our knowledge, this is the first case of photocatalytic reduction of uranium by D-A-type organic photocatalysts at such a low pH. Apparently, the current work has taken a crucial step in the application of photocatalytic technology to the field of strongly acidic radioactive wastewater treatment.

2. Experimental section

2.1. Chemicals

Anhydrous sodium acetate (99%), lactic acid (LA, 90%), ascorbic acid (AA, 95%), isopropyl alcohol (*i*-PrOH, 99.5%), 2,6-dibromoanthracene (98%), 2,6-dibromoanthracene-9,10-dione (98%), potassium carbonate (99%), N,N-Dimethylformamide (99.8%), tetrakis (triphenylphosphine)palladium, uranyl nitrate hexahydrate (99%), arsenazo III (95%) and chloroacetic acid (99%) are purchased from Alfa Aesar Ltd. 4-hydroxy-2,2,6,6-tetramethyl-piperidinooxy (TEMPO, 99%), 5,5-Dimethyl-1-pyrroline-N-oxide (DMPO, 97%), tertiary butanol (TBA, 99.8%), potassium bromate (KBrO$_3$, 99.8%), methyl alcohol (CH$_3$OH, 99.8%) and 1,4-benzoquinone (*p*-BQ, 98%) are acquired from Sinopharm Chemical Reagent Co, Ltd. The target monomer of 2,5,8,11-
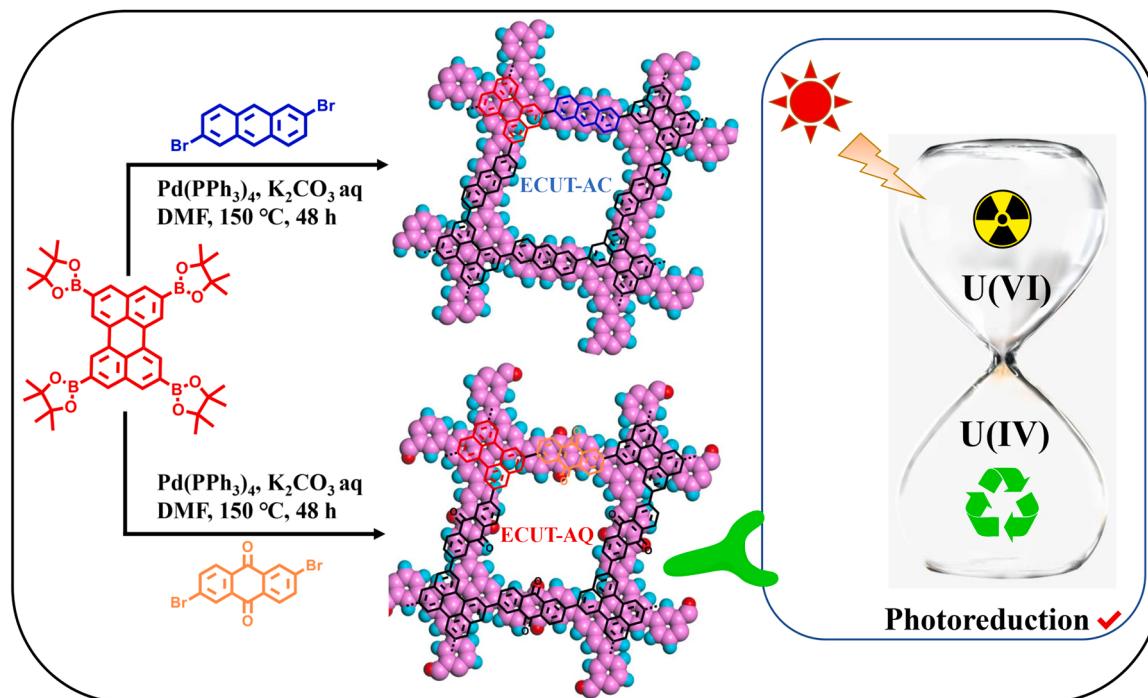
Scheme 1. Chemical structures of the monomers, and the preparation of **ECUT-AC** and **ECUT-AQ** through Suzuki-Miyaura cross-coupling polycondensation.

tetrakis(4,4,5,5-tetramethyl-1,3,2-dioxaborolan-2-yl)perylene is synthesized according to the method reported by the predecessors [31,39] (see Supporting Information for details). The ultrapure water (18.25 MΩ cm) is applied as experiments water from a Millipore Milli-Q system. All reagents are used without further purification unless otherwise stated.

2.2. Sample characterization

The synthesized monomer is checked with ^1H NMR and ^{13}C NMR spectra which are implemented on Bruker AM-400 MHz. FT-IR spectra are calendared with a Bruker TENSOR 27 instrument. UV–vis diffuse reflection spectrum (DRS) is received with UV–vis spectrophotometer (UV-2550, Shimadzu, Japan). Routinely, the photoluminescence spectra (PL) are cassetted on a spectrophotometer (Edinburgh FI/FSTCSPC 920). The corresponding time-resolved transient PL decay (TR-PL) spectras are carried on Edinburgh Instruments FLS 920 fluorescence spectrophotometer. The contact potential difference (CPD) measurements are carried out on a commercial Bruker AFM in an air atmosphere with an imaging mode of AM-KPFM. Powder X-ray diffractions (PXRD) data are obtained on a Bruker AXS D8 Advance A25 powder X-ray diffractometer (40 kV, 40 mA) using Cu Kα (λ = 1.5406 Å) radiation. X-ray photoelectron spectroscopy (XPS) spectra are gathered with a Thermo VG Multilab 2000X with Al Kα irradiation. The solid-state ^{13}C NMR spectra are obtained on the Bruker Advance 600 MHz spectrometer. Element analysis (EA) is obtained by a Vario EL analyzer. N_2 adsorption and desorption isotherms are carried out at 77 K with a micromeritics ASAP 2020 M system. The **ECUT-AC** and **ECUT-AQ** samples are outgassed for 12 h at 120 °C under vacuum prior to the gas adsorption studies. The surface areas are evaluated using Brunauer-Emmett-Teller (BET) model applied between P/P_0 values of 0.05 and 0.20. The pore size distributions are calculated using the non-localized density functional theory (NLDFT) method. Electron spin resonance (ESR) is used to investigate the reactive species, which is recorded using a Bruker A300 spectrometer. Specifically, the 5,5-dimethyl-1-pyrroline-N-oxide (DMPO) is used to trap the superoxide radical ($\cdot O_2^-$) and hydroxyl radicals ($\bullet OH$). As well, 4-hydroxy-2,2,6,6-tetramethyl-piperidinooxy (TEMPO) is a typical electron capture agent, which can be reduced to produce an ESR-silent product (TEMPOH). Inductively coupled plasma-mass spectrometry (ICP-MS) is used to determine the concentrations of interfering metal ions and the residual Pd content of CMPs. All electrochemical experiments are performed according to reported methods, (see supporting information for details).

2.3. Typical procedure for the synthesis of ECUT-AC and ECUT-AQ

2.3.1. ECUT-AQ

A mixture of 2,5,8,11-tetrakis(4,4,5,5-tetramethyl-1,3,2-dioxaborolan-2-yl)perylene (378.22 mg, 0.5 mmol), 2,6-dibromoanthracene-9,10-dione (363.87 mg, 1.0 mmol) and $Pd(PPh_3)_4$ (14.5 mg, 0.013 mmol) are dissolved in 20 mL DMF. After K_2CO_3 aqueous solution (2.0 M, 2.0 mL) is added, the mixture is degassed by freeze-pump-thaw cycles and filled back with nitrogen. Then the reaction mixture is stirred for 48 h at 150 °C. After cooling to RT, the resulting mixture is irrigated into H_2O (100 mL). The solid product is gathered, and sequentially washed with water, acetone, dichloromethane, tetrahydrofuran, then dried under vacuum at 120 °C overnight. Orange red powder is obtained (yield, 92%). Anal. Calcd for $(C_{76}H_{32}O_8)_n$ (%): C, 85.06; H, 3.01. Found : C, 75.46; H, 4.94. The residual Pd content is found to be 0.42 wt % from ICP-MS.

ECUT-AC is synthesized and purified according to the similar procedure of **ECUT-AQ**, except that the monomer 2,6-dibromoanthracene-9,10-dione (363.87 mg, 1.0 mmol) is replaced by 2,6-dibromoanthracene (333.90, 1.0 mmol). Yellow powder is obtained (yield, 95%). Anal. Calcd for $(C_{76}H_{40})_n$ (%): C, 95.77; H, 4.23. Found : C, 89.27; H, 5.54. The residual Pd content is found to be 0.34 wt% from ICP-MS.

2.4. Photocatalytic reduction of UO_2^{2+} experiments

Batch photocatalytic experiments are carried out in a jacketed quartz beaker photoreactor (instrument model: CEL-APR250H), and the reaction temperature is maintained at RT (20 ± 2 °C) by a water-cooling system. Typically, 25 mg **ECUT-AQ** (or **ECUT-AC**) is dispersed 100 mL 50 ppm U(VI) aqueous solutions with 200 mg ascorbic acid (AA) and under stirring continuously. After stirred in the dark for 60 min to reach adsorption-desorption equilibrium, then the suspension is immediately irradiated using a 300 W Xe lamp (Light source model: SHX-F300, λ ≥ 400 nm). To analysis the uranium concentration, aliquot (~ 2 mL) of the suspension is pipetted at given times and filtered with 0.22 μm polyether sulfone filters. The filtrate is collected and detected with UVmini-1240 by arsenazo-III spectrophotometric technology at 652 nm to determine the remaining uranium content. This measured absorbance with illumination time is converted to photoreduction efficiency of uranium in accordance with the Eq. (1):

$$RE = \frac{(C_0 - C_t)}{C_0} \times 100\% \tag{1}$$

where RE is uranium reduction efficiency, C_0 is initial concentration of uranium (ppm or mg L^{-1}), and C_t is the concentration of uranium (ppm or mg/L) at time, respectively.

In the pH-dependent experiments, the initial pH of solution is adjusted with negligible volume of NaOH (0.1 M) or HNO_3 (0.1 M) solution. In the recycling experiments, the reacted suspension is centrifuged to remove the supernatant. Then, the photocatalyst is retrieved by immersing in 1 M NH_4HCO_3 with vigorous stirring for 24 h to release uranium. After further washed with deionized H_2O, the **ECUT-AQ** is used for the next cycle of photocatalytic testing.

2.5. DFT calculation methods

All density functional theory calculations are carried out with the Gaussian 16 program package [46]. Empirically, optimization of all geometries and frontier molecular orbitals at the CAM-B3LYP/6–31 G (d) theoretical level using Gaussian 16 [34,47]. The relevant specific methods are discussed in detail in the Supporting Materials.

3. Results and discussion

3.1. Molecular design and synthesis

Compared with anthracene unit, anthraquinone unit not only exhibits unique redox activity, but also has stronger electron withdrawing. Therefore, constructing an anthraquinone-based polymer is conducive to achieving better photocatalytic activity. To this end, the **ECUT-AC** and **ECUT-AQ** are synthesized via Pd(0)-catalyzed Suzuki-Miyaura-type polycondensation of 2,5,8,11-tetrakis(4,4,5,5-tetramethyl-1,3,2-dioxaborolan-2-yl)perylene with non-redox activity 2,6-dibromoanthracene or redox-active 2,6-dibromoanthracene-9,10-dione monomers (as depicted in Scheme 1). Certainly, both resulting CMPs with the cross-linking networks are insoluble, chemically stable, amorphous nature (Fig.S1a) and also reveal high thermal stability with a higher decomposition temperature (about 600 °C) under N_2 atmosphere (Fig.S1b).

3.2. Characterization of samples

Moreover, observing from the scanning electron microscope image (Fig. 1a and b), both of the **ECUT-AC** and **ECUT-AQ** possess aggregated sheet structure. Subsequently, their fine chemical structure and composition are fully characterized via FT-IR, solid-state ^{13}C NMR spectra and XPS. Seen from the FTIR (Fig. 1c), the characteristic vibration peak at 1673 cm^{-1} assigned to keto group (C = O) are presence in ECUT-AQ, while the absent in ECUT-AC, manifesting the successful
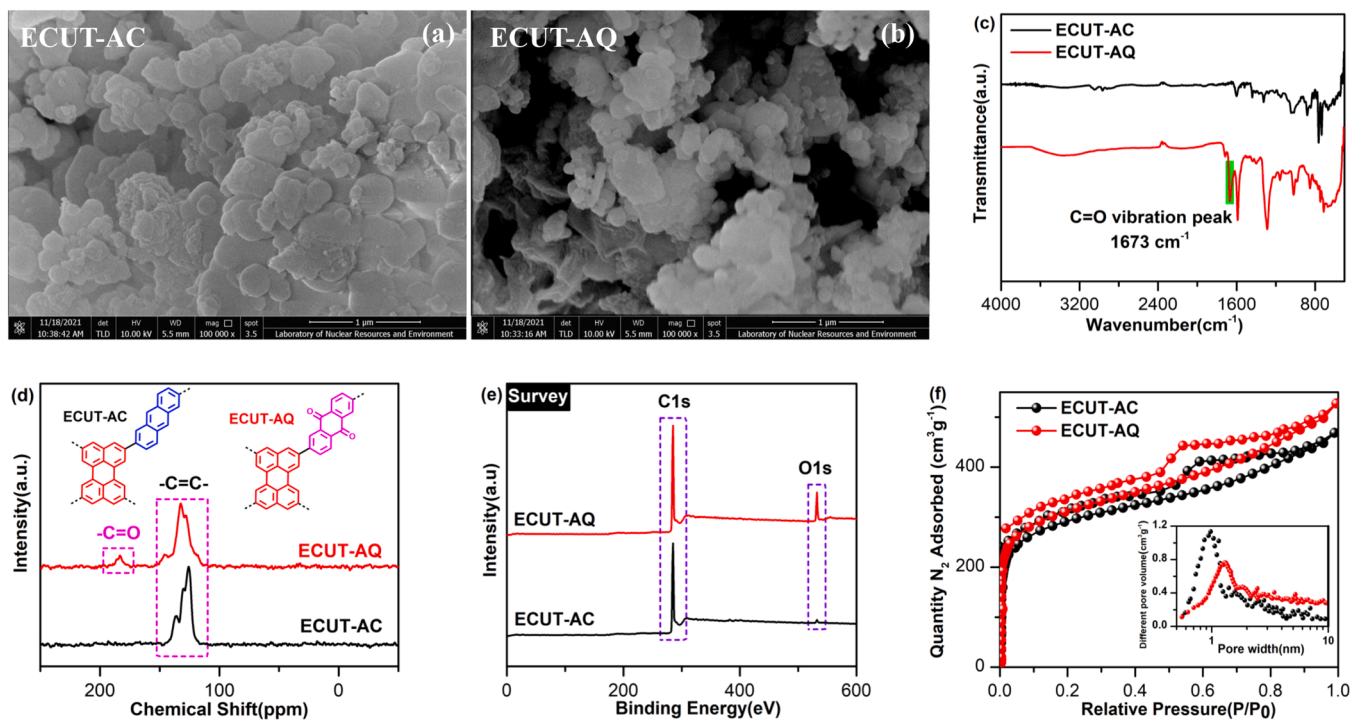
Fig. 1. (a, b) SEM images for **ECUT-AC** and **ECUT-AQ**; (c) FT-IR spectrum of **ECUT-AC** and **ECUT-AQ**; (d) The ^{13}C NMR spectrum (solid-state) spectrums of **ECUT-AC** and **ECUT-AQ**; (e) XPS survey spectra of **ECUT-AC** and **ECUT-AQ**; (f) Nitrogen adsorption/desorption curves at 77 K; and the corresponding pore size distribution curves of **ECUT-AC** and **ECUT-AQ** via NLDFT calculation (inset).

coupling, and the redox activity AQ moiety is well preserved in ECUT-AQ. As for the solid-state ^{13}C NMR spectra (Fig. 1d), signals in the range of 110–150 ppm for **ECUT-AQ** and **ECUT-AC** are accountable for the aromatic carbons (C = C). Importantly, a distinguished signal at 183 ppm in **ECUT-AQ** is attributed to the C = O and certainly supports the existence of carbonyl carbon, further demonstrating the successful introduction of the AQ moiety. This is also consistent with the information obtained by FTIR. Additionally, the XPS survey spectra indicates (Fig. 1e) the main chemical components of **ECUT-AC** and **ECUT-AQ** are C and C, O, respectively. To sum up, these evidences demonstrated the successful preparation of **ECUT-AC** and **ECUT-AQ**.

3.3. Specifc surface area and pore size distribution

Furthermore, the porous nature of **ECUT-AC** and **ECUT-AQ** are investigated via the nitrogen adsorption/desorption isotherms which is recorded at 77 K. Seen from (Fig. 1f) and Table S1, both of the obtained polymers contain abundant micropores, which are well-documented by nitrogen adsorption isotherm curve rises sharply at low relative pressures. Correspondingly, as shown in the pore size distribution curve (Fig. 1f inset), the CMPs are mainly microporous (approximately 1.0 nm in diameter), and some mesoporous can also be clearly resolved. Notably, contrast to **ECUT-AC** (1044.2 m^{2}g^{-1}), the **ECUT-AQ** (1157.6 m^{2}g^{-1}) demonstrates a larger BET, proving that replacing AC with AQ in the polymer backbone helps to increase the BET. Generally, the CMPs with larger BET can provide more catalytic active sites and improve photocatalytic performance.

3.4. Optical performance and energy band structure

To intuitively investigate the optical absorption properties of **ECUT-AC** and **ECUT-AQ**, their UV–vis DRS spectra are estimated in the solid powder state. Seen from Fig. 2a, both **ECUT-AC** and **ECUT-AQ** display wide and powerful visible-light absorption in the range of 400 − 800 nm because their large π-conjugated backbones. Notably, the absorption

maximum of ca. 537 nm for **ECUT-AQ** is significantly bathochromic-shifted by ca. 82 nm over that of ca. 455 nm for **ECUT-AC**, which can be attributed to integration of AQ monomer as a stronger acceptor, greatly facilitating D-A intramolecular charge transfer (ICT) from perylene to AQ. The corresponding apparent color deepens from yellow to orange-red (inset in Fig. 2a). Correspondingly, the optical bandgaps (E_g) of ECUT-AC and ECUT-AQ calculated from the Tauc plots (Fig. 2b) are 2.32 and 1.98 eV, respectively. Furthermore, the oxidative half cyclic voltammograms (C-V) of **ECUT-AC** and **ECUT-AQ** are carried out in CH_3CN to determine their HOMO levels. Ferrocene/ferrocenium (Fc/Fc$^+$) as an internal reference and 0.1 M tetra-n-butylammonium hexafluorophosphate (TBAPF$_6$) as supporting electrolyte. The HOMO energy levels (E_{HOMO}) are calculated from onset redox potentials according to the equation of $E_{HOMO} = -(E_{ox\_onset} + 4.8 \text{ eV vs. Ag/AgCl} - E_{Fc/Fc+}^{ox})$, and $E_{Fc/Fc+}^{ox}$ (0.389 eV vs. Ag/AgCl in the present work, Fig.S2a) is the redox potential of ferrocene/ferrocenium (Fc/Fc$^+$) couple for the calibration. As shown in Fig.S2b, the corresponding values of E_{HOMO} are − 5.67 (+1.17) and − 5.58 eV (+1.08 V) vs. vacuum (vs. SHE) for **ECUT-AC** and **ECUT-AQ**. The LUMO levels are then calculated from the equation of $E_{LUMO} = E_{HOMO} + E_g$ and the corresponding data are − 3.35 (−1.15) and − 3.60 eV (−0.90 V) vs. vacuum (vs. SHE) for **ECUT-AC** and **ECUT-AQ**, respectively. The more negative LUMO position of polymers as compared to the U(VI)/U(IV) reduction potential (UO$_2^{2+}$/UO$_2$: 0.441 and UO$_2^{2+}$/U^{4+} 0.267 vs. SHE [31,32]) illustrates thermodynamic feasibility for the reduction reaction of U(VI) to U(IV). The corresponding energy level diagram is shown in Fig. 2c. Therefore, constructing the D-A polymer with AQ as the acceptor is mainly to lower the position of LUMO, thereby narrowing the band gap and exhibiting excellent visible light harvesting performance, thus prospectively improving photocatalytic activity.

3.5. Electron transfer dynamics

Routinely, the photogenerated charges recombination behavior is intuitively characterized by PL spectroscopy. As shown in Fig. 3a, the **ECUT-AC** and **ECUT-AQ** possess distinct fluorescent emission peaks and
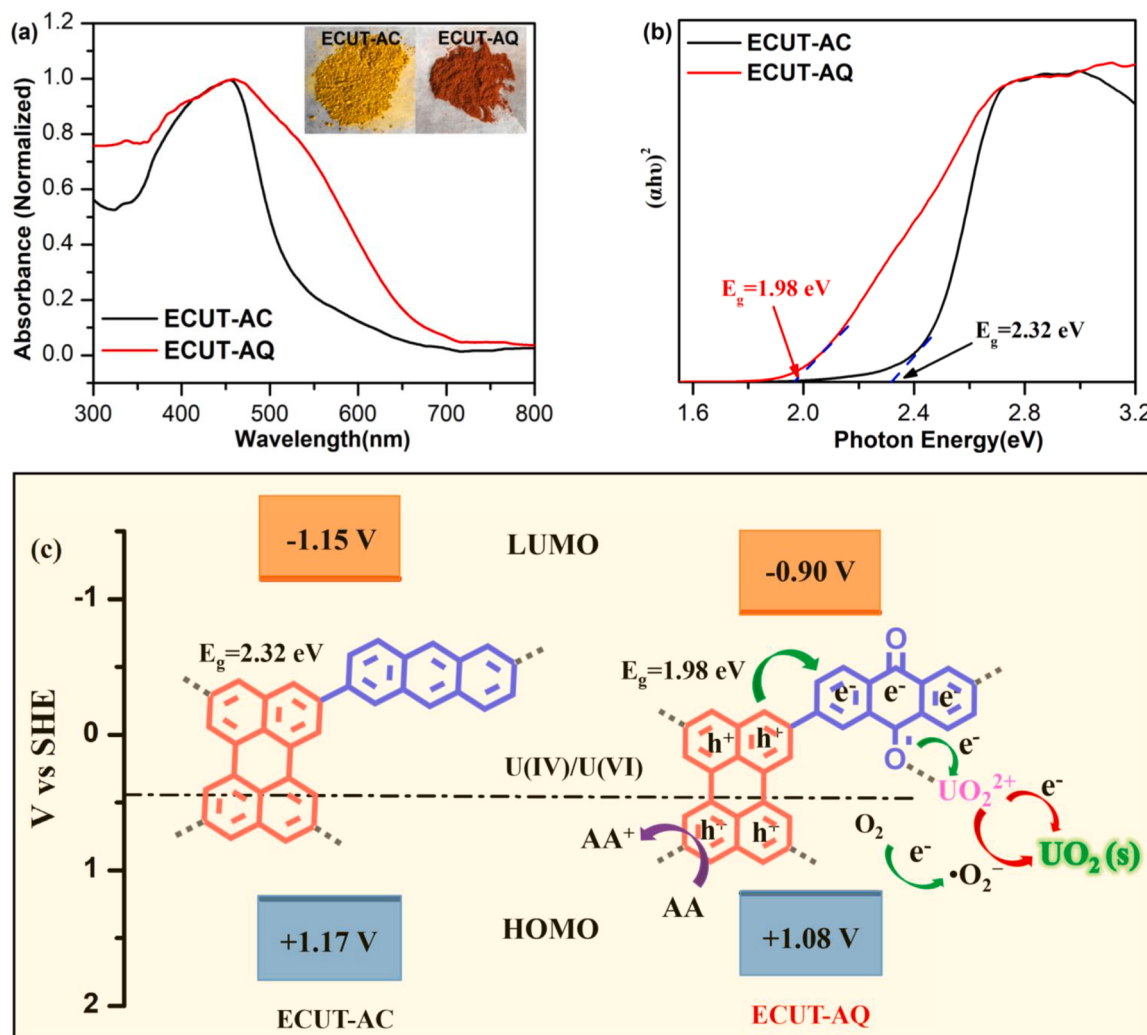
Fig. 2. (a) UV-Vis DRS spectra of **ECUT-AC** and **ECUT-AQ**; inset: apparent color (b) the bandgaps of **ECUT-AC** and **ECUT-AQ** calculated by Tauc-Plot; (c) Energy band diagram of **ECUT-AC** and **ECUT-AQ**.

intensities despite similar molecular skeleton structure. The anthraquinone-based polymer **ECUT-AQ** displays a noticeable redshifted emission locates at 637 nm with much lower peak intensity than that of **ECUT-AC** (the maximum emission peak: 565 nm), certificating that D–A type **ECUT-AQ** with a redox-active AQ unit can suppress radiative recombination effectively, which endows higher photocatalytic activity. Furthermore, the time-resolved transient PL decay spectra (TR-PL), transient current responses (I–t) and electrochemical impedance spectra (EIS) are monitored to evaluate the separation and transfer rate of photogenerated electron-hole pairs. As presented in Fig. 3b and Table S2, the weighted mean lifetimes of photogenerated electrons (τ_1) for **ECUT-AQ** is 1.14 ns, which is significantly longer than that of **ECUT-AC** (0.92 ns), suggesting that the integration of AQ as acceptor can reduce the probability of photo-induced electron deactivation, thereby improving the photocatalytic activity. Additionally, as revealed by i-t curve (Fig. 3c), the **ECUT-AQ** (0.729 µA cm^{-2}) displays a much higher photocurrent density than that of **ECUT-AC** (0.118 µA cm^{-2}), proclaiming that much more photoinduced electrons can be generated during the photocatalytic reaction of **ECUT-AQ**, which has a great contribution to photocatalytic uranium reduction process. Meanwhile, it can be seen from the EIS curves (Fig. 3d) that the arc radius of **ECUT-AQ** is much smaller than that of **ECUT-AC**, demonstrating better interfacial charge transfer kinetics, which favorably supports the results of

photocurrent measurements. Normally, the concentration of photoinduced holes are intuitively plumbed by contact potential difference (abbreviated as CPD) technique. Seen from the steady state CPD images of **ECUT-AC** and **ECUT-AQ** in dark and illumination at 450 nm (Fig. 3e), both of the samples achieve a significant raise in CPD values under illumination, implying photoinduced h$^+$ is migrated rapidly to the photocatalyst surface and abruptly accumulated. Particularly, the **ECUT-AQ** achieves a larger ΔCPD amplitude of 198 mV than that of **ECUT-AC** (54 mV), certificating that photogenerated charge separation and transfer can be facilitated by constructing D-A conjugated polymers containing AQ groups.

Known from the previously reported literature [48–51], the built-in electric feld magnitude (abbreviated as F_s) is a primary kinetic factor affecting charge separation. The F_s value is calculated by the equation S2 in the Supporting Information. The equation reveals that the F_s value is mainly determined by the charge density (ρ) and the surface voltage (V_s) because $\mathcal{E}$ and $\mathcal{E}_0$ are two constants. As shown in Fig. 3f, the surface charge densities of **ECUT-AC** and **ECUT-AQ** are 0.659 and 8.144 µA cm^{-2}, respectively; the corresponding surface voltages are 54 and 198 mV, respectively. It can be found that the F_s value of **ECUT-AQ** is bout 6.73 times that of **ECUT-AC**, which further confirmed that the **ECUT-AQ** has a more effective separation of photogenerated electron-hole pairs.
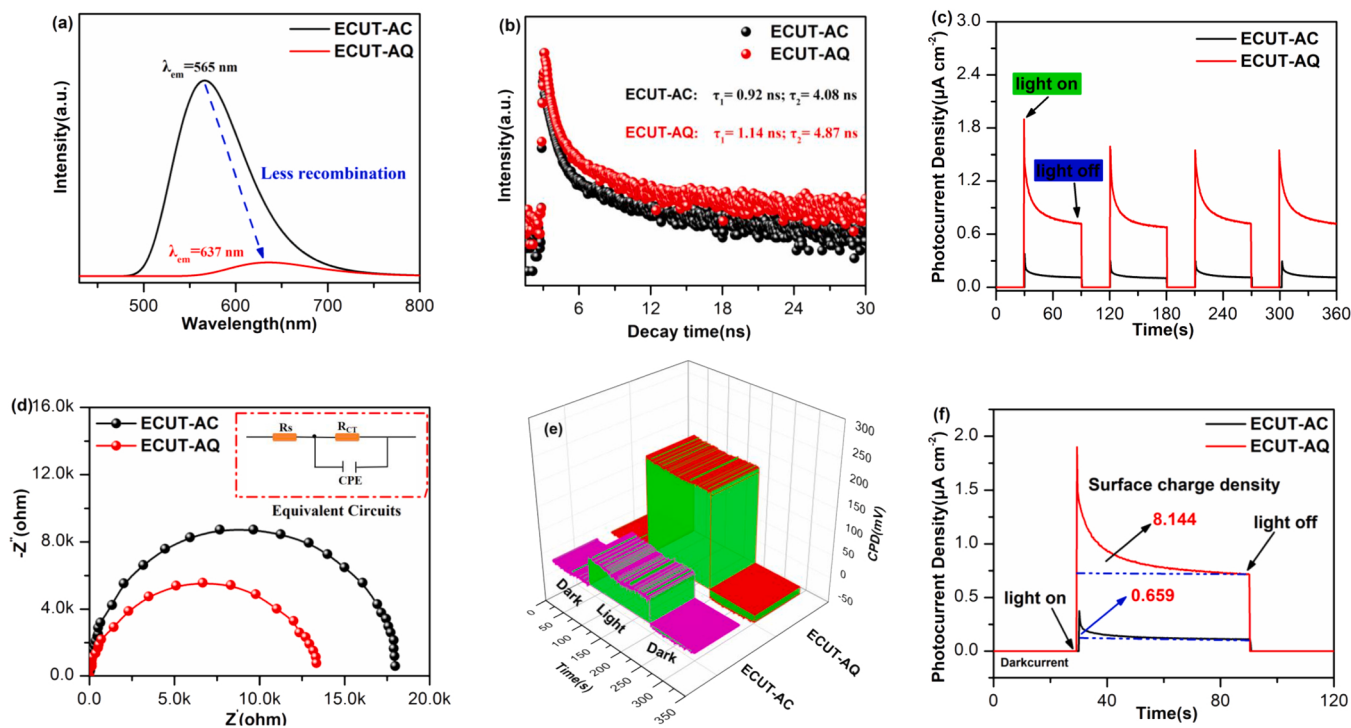
Fig. 3. (a) Photoluminescence spectra of **ECUT-AC** and **ECUT-AQ** under 420 nm excitation; (b) (c) Transient current responses to on–off cycles of illumination on **ECUT-AC** and **ECUT-AQ** membrane electrodes (0 bias) in 0.5 M Na$_2$SO$_4$; (d) EIS Nyquist plots of **ECUT-AC** and **ECUT-AQ** at open circuit voltage; (e) Contact potential difference (CPD) of the resulting CMPs in the dark and under illumination at 450 nm; (f) The surface charge density of **ECUT-AC** and **ECUT-AQ**.

3.6. The density functional theory (DFT) calculations

Besides, the intramolecular excited electron-transfer process and interface interaction of photocatalysts are systematically investigated using the DFT calculations.

The results of frontier molecular orbital distribution are shown in Fig. 4a. As for **ECUT-AC**, both highest occupied molecular orbital (HOMO) and lower unoccupied molecular orbital (LUMO) are mainly distributed on the polymer backbone. Comparatively, the HOMO for **ECUT-AQ** is delocalized over the donor segment (perylene uint), while the LUMO is delocalized over the acceptor segment (AQ unit), conforming to the characteristics of D-A structure, which is favorable for spatial charge separation via HOMO-LUMO transition. Likewise, the molecular dipoles and Mulliken atomic charges of the respective polymer molecules are obtained directly from DFT calculation as depicted in Fig. 4b. According to the calculated results, on one hand, the **ECUT-AQ** with higher electronegativity monomer presents a larger dipole value of 0.9585 Debye than that of **ECUT-AC** (0.0619 Debye). Ordinarily, the larger molecular dipole of the D–A system ensures a sufficiently large built-in electric feld, which is beneficial for photogenerated e⁻-h⁺ pair separation, thus enhancing the photoreduction activity. Predictably, the built-in electric field of AQ-integrated **ECUT-AQ** is significantly enhanced, which is consistent with the experimental results. Obviously, on the other hand, the O atom has the most negative value of Mulliken atomic charges for all atoms of AQ containing polymer (**ECUT-AQ**), exhibiting the reddest color in the Mulliken charges map. According to the hard-soft-acid-base theory, stronger coordination occurs between the more negatively charged oxygen and the positively charged hexavalent uranyl ion (UO$_2^{2+}$). As a result, as shown in Fig. 4c, the **ECUT-AQ** (55.8 kcal/mol) achieves larger binding energy for anchoring UO$_2^{2+}$ than that of **ECUT-AC** (49.3 kcal/mol), which is beneficial to promote interface electron transfer, that is, the uranyl ions more efficiently accept electrons from the photocatalyst and are reduced more efficiently.

3.7. Photocatalytic performance and stability

Conventionally, in the photoreduction uranium system, three main operating parameters, namely pH value, sacrificial agents and initial concentration of uranyl ions, need to be intensively optimized. In particular, during photocatalytic process, the existence form of U(VI), photocatalyst surface properties, and subsequent interaction with UO$_2^{2+}$ are strongly correlated with pH value. As depicted in Fig. 5a, for **ECUT-AC**, when the pH decreased from 5 to 1, the adsorption and photoreduction activity of U(VI) also degenerate, and when the pH is 1, the corresponding uranium removal activity is negligible. In contrast, the photoreduction of U(VI) by **ECUT-AQ** has no signifcant change at given pH values, and optimum uranium removal (73%) is obtained at pH 4 (irradiation for 60 mins). Unexpectedly, under strong acidity (pH=1, irradiation for 60 mins), a uranium removal rate of 65% is still achieved, among which the dark state adsorption of uranium is 15.3%, and the photocatalytic reduction of uranium is 49.7%. A possible explanation for this unusual but fascinating experimental result is that (as shown in Fig. S3): as a redox active unit, AQ is reduced to oxanthranol (OAO) by the electrons (a certain amount of H⁺ coexistence is required), and the OAO formed is subsequently oxidized to AQ by the holes. Unequivocal, the above-mentioned process can facilitate the migration of photogenerated electrons and effectively promote the photoreduction activity of uranium under strong acid conditions.

Generally, sacrificial agents (SA) which can timely consume h⁺ and powerfully block the recombination of photoinduced e⁻ and h⁺ are critical for achieving perfect photoreduction of uranium. As expressed in Fig. 5b, in the absence of SA, uranium removal is negligible for both samples. Obviously, among several common sacrificial agents (MeOH, EtOH, *i*-PrOH, LA and AA), AA as a sacrificial agent achieves the best uranium removal (9.1% and 86% for **ECUT-AC** and **ECUT-AQ**, respectively), probably due to its high reduction potential and strong affnity for perylene unit. In addition, the photoreduction activity under variable initial U(VI) concentrations is evaluated, and the optimal initial uranium concentration is 50 ppm (Fig.S4).
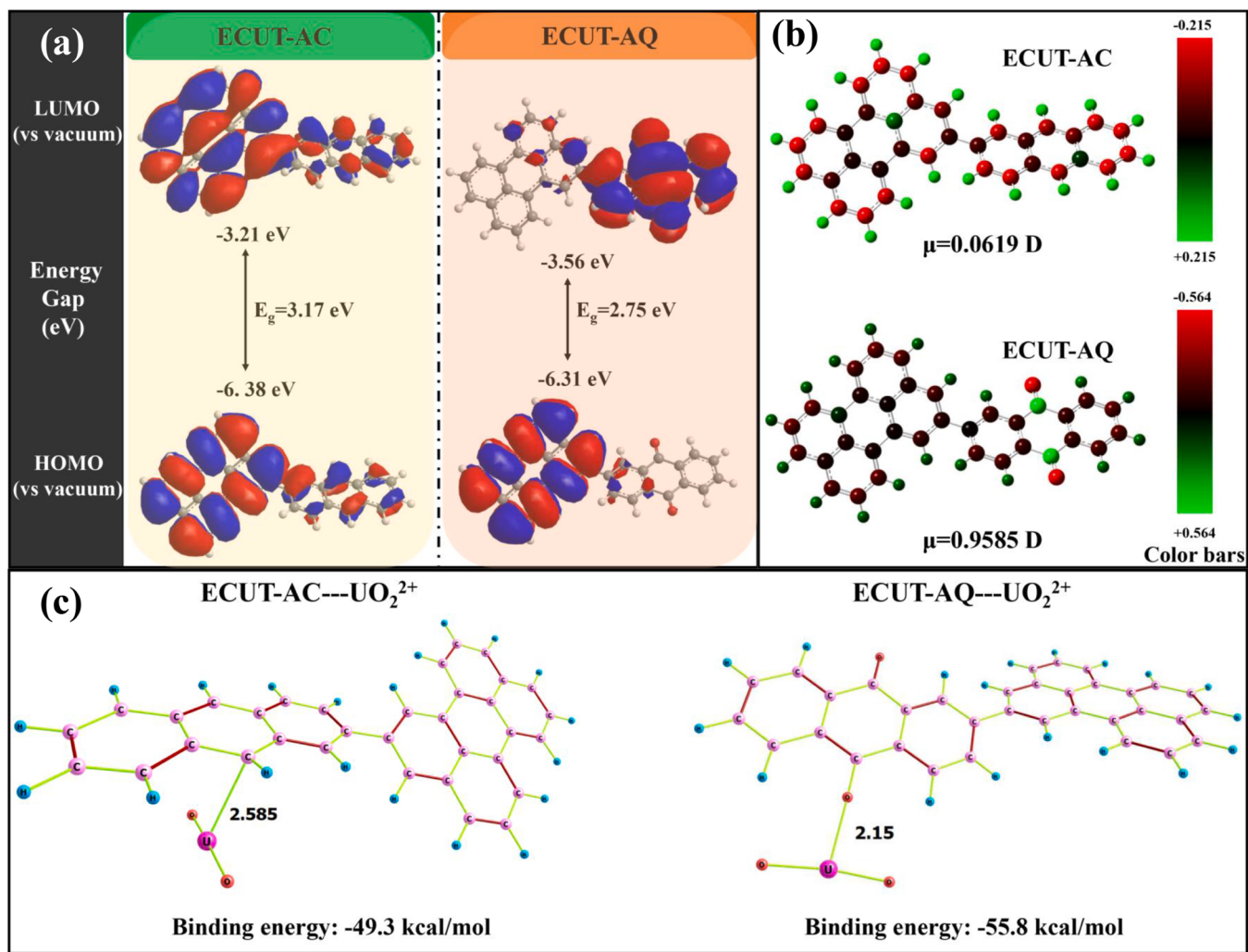
Fig. 4. (a) The HOMO and LUMO orbital distributions of the simplified copolymer fragment from DFT simulation; (b) The Mulliken atomic charges of every atom in **ECUT-AC** and **ECUT-AQ**, and the corresponding dipole moments (μ: the unit of dipole moment is Debye) of **ECUT-AC** and **ECUT-AQ**; (c) The optimal structure after adsorbing UO_2^{2+} and the corresponding adsorption energy.

Subsequently, we investigated the effect of AQ groups on photoreduction activity of uranium in strongly acidic solution (pH=1) under the same parameters (25 mg photocatalyst, AA as SA, 100 mL, 50 ppm UO_2^{2+}). As shown in Fig. 5c, the U(VI) removal rates are 1.5% and 15% for **ECUT-AC** and **ECUT-AQ**, respectively, after 60 mins of dark state adsorption. The results show that the integration of AQ enhances the coordination adsorption to uranyl ions and promotes the interfacial transfer of photogenerated electrons. After reaching the adsorption-desorption equilibrium, continuous visible light irradiation ($\lambda \geq 400$ nm) for 120 mins, the U(VI) removal rates increased significantly to 9.1% and 86% for **ECUT-AC** and **ECUT-AQ**, respectively. According to the pseudo first-order equation (Fig. 5d), the corresponding photoreduction reaction rate constants (k) are 0.0007 and 0.015 min^{-1}, respectively. The above experimental results show that such outstanding photocatalytic activity of **ECUT-AQ** in strongly acidic solution is mainly attributed to the following three points: (1) AQ is a good electron-deficient acceptor and constitutes the D-A system. On the one hand, it can promote the ICT process in **ECUT-AQ** and broaden the visible light absorption range; on the other hand, it can generate a huge built-in electric field and promote the effective separation of electron-hole pairs; (2) AQ has unique redox properties, which can further facilitate charge transmission along the polymer backbone as an electron transfer channel; (3) AQ contains two oxygen atoms with high electronegativity, which can enhance the coordination adsorption with uranyl ions and

further promote the transfer of electrons from the photocatalyst surface to uranyl ions. Notably, this is the first example of efficient uranium reduction under strong acid conditions based on D-A-type CMPs photocatalysts.

Reusability and selectivity are two crucial metrics for comprehensively evaluating the utility of photocatalysts. Seen from Fig. 5e, no significantly diminished is found in the photoreduction activity of uranium after five runs, which indicates the wonderful stability and reusability of **ECUT-AQ**. Considering the practicability in real uranium-containing wastewater, the photoreduction activity of uranium has been investigated in multi-ion solutions, including Na^+, Cs^+, VO_2^+, Mg^{2+}, Sr^{2+}, Zn^{2+}, Co^{2+}, Ni^{2+}, Ca^{2+}, Dy^{2+}, Al^{3+}, Er^{3+} and Yb^{3+}, with their molar concentrations ratio is 50:1 (M^{n+}/U(VI)). As revealed in Fig. 5f, the **ECUT-AQ** can still exhibits perfect photoreduction activity of U(VI) after irradiation, demonstrating that admirable uranium selectivity can be achieved through the participation of photogenerated electrons.

3.8. Mechanism analysis

Importantly, the exact species of uranium present after photocatalytic reduction is crucial for further optimizing the U(VI) reduction performance and in-depth dissecting the U(VI) conversion mechanism. As yet, popular opinion tacitly acknowledges the generation of U(IV),
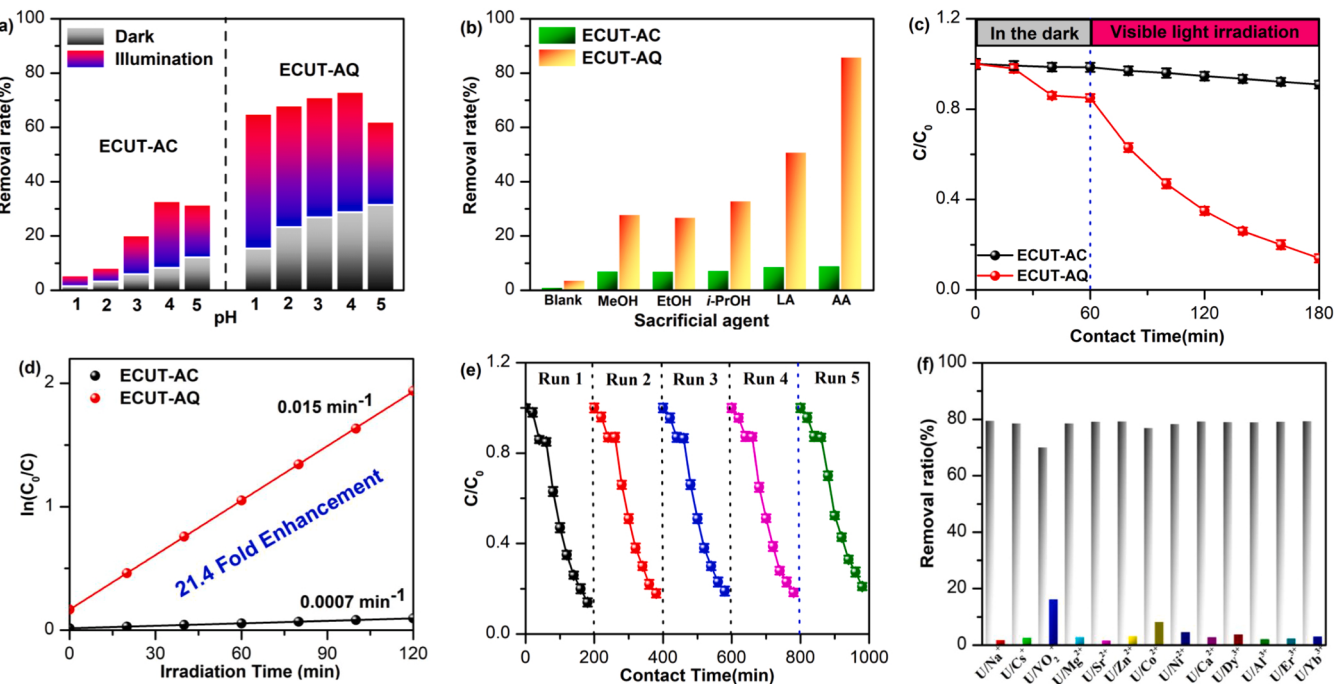
Fig. 5. (a) Effect of pH on U(VI) reduction removal for obtained CMPs; (b) Effect of different sacrificial agents on U(VI) reduction removal for obtained CMPs; (c) The variation of UO_2^{2+} concentration vs. illumination time with CMPs as photocatalysts; and (d) The corresponding pseudo-first-order rate constant (*k*) of UO_2^{2+} reduction; (e) Cycling performance of **ECUT-AQ**; (f) Effects of other competitive ions on photocatalytic removal of uranium for **ECUT-AQ** (Reaction conditions: 100.0 mL 50.0 ppm U(VI) containing 200 mg AA, $M^{n+}/U= 50.0:1.0$) at pH 1.0, 25 mg **ECUT-AQ** under visible light).

but no agreement has been achieved on the exact species. Therefore, FTIR, XRD and XPS characterizations of the reacted sample are carried out to determine the oxidation state of surface uranium species after illumination and the interaction between UO_2^{2+} ions and **ECUT-AQ**. Fig. 6a presents the FTIR of ECUT-AQ before and after U(VI) photoreduction. After irradiation, an obvious O = U = O antisymmetric vibration peak (at 933 cm^{-1}) is observed in the ECUT-AQ, indicating that uranium-

containing substances are newly formed on its surface. Afterward, XPS technology is utilized to further parse the valence states of the resulting uranium species. As can be seen from Fig. 6b and Table S3, O 1s high-resolution XPS spectra of fresh **ECUT-AQ** can be deconvoluted into two peaks at 532.96 and 531.90 eV, which can be assigned to absorbed H_2O (or O_2) and C = O band, respectively. Obviously, the two peaks positions are significantly shifted by ~0.3 eV towards higher binding
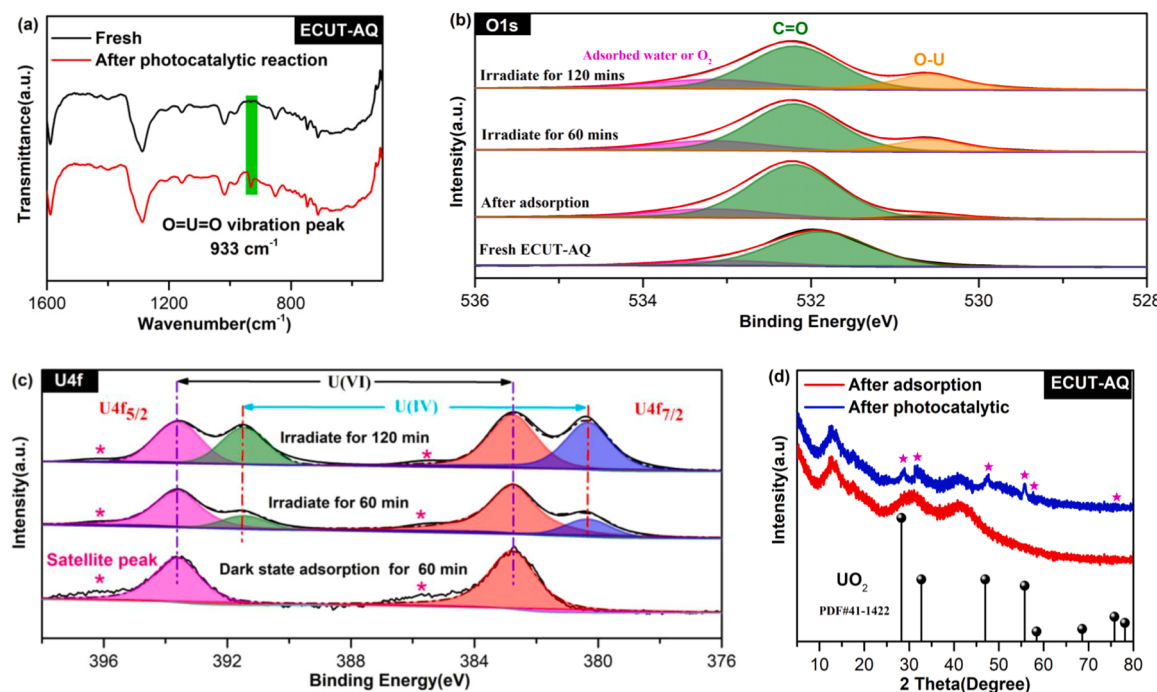
Fig. 6. (a) The FT-IR of **ECUT-AQ** after photocatalytic reduction of uranium; (b) High-resolution O1s and (c) U 4 f XPS spectra of **ECUT-AQ** after different reaction times; It should be pointed out that: "*" represents satellite peaks; (d) The XRD of **ECUT-AQ** after photocatalytic reduction of uranium.

energy after adsorption of U(VI), indicating that O in the carbonyl group is involved in the uranium coordination adsorption. Moreover, a new O-U characteristic peak at approximately 530.60 eV appeared after the reaction, and the corresponding peak area increases significantly with the prolongation of illumination time, indicating that the photocatalytic process may contribute to the formation of new uranium-containing oxides. To illustrate the above conjecture, the U 4 f high-resolution XPS testing of the adsorbed and photo-reduced uranium on **ECUT-AQ** is performed (Fig. 6b, Fig.S5 and Table S4). For **ECUT-AQ** after adsorption of U(VI), the distinctive peaks located at 393.61 and 382.76 eV are earmarked to U 4 $f_{5/2}$ and U 4 $f_{7/2}$ of U(VI), respectively, which strongly certificating that UO_2^{2+} is indeed adsorbed on the polymer surface. Interestingly, the U 4 f spectra of U(VI)-accumulated **ECUT-AQ** after irradiation can be deconvolved into four peaks compared to the dark state. The two newly emerged characteristic peaks at 391.44 and 380.32 eV are delimited as U 4 $f_{5/2}$ and U 4 $f_{7/2}$ of U(IV), respectively. Notably, the corresponding ratio of U(IV)/U(VI) is increased from 0.42 to 1.02 as the irradiation times is prolonged from 60 to 120 mins, suggesting that new U(IV) species are formed under illumination, and the amount of U(VI) photoreduced to U(IV) increased with prolonged illumination time. In addition, XRD test is performed to determine exactly what the resulting tetravalent species is. As shown in XRD pattern of **ECUT-AQ** after photocatalytic reaction (Fig. 6d), some additional signals located at ~28.3°, 32.7°, 47.0°, 55.8° and 78.1° are discovered, which are in perfect agreement with the diffraction signature of crystalline uranium dioxide (UO_2) (UO_2: PDF#41–1422), proving that uranyl ions are photocatalytically reduced to finally form UO_2 nanoparticles.

The effect of various reactive species (such as h^+, e^-, •OH and •O_2^- radicals) on photoreduction of U(VI) by **ECUT-AQ** are comparatively investigated to better clarify the photocatalytic mechanism. In typical quenching experiments, the AA, $KBrO_3$, TBA and *p*-BQ are used as scavenger for h^+, e^-, •OH and •O_2^-, respectively. Seen from Fig. 7a, the photoreduction activity of U(VI) is remarkably ameliorated in the present of AA, which can be attributed to the fast and efficient trapping of

photogenerated holes by AA, thus improving the separation efficiency of e^- / h^+ pairs. Then, the addition of TBA has little effect on photoreduction of U(VI), revealing •OH active species play no role in photocatalysis process. Instead, the presence of $KBrO_3$ and *p*-BQ will significantly inhibited photo-reductive removal of U(VI), demonstrating that the photogenerated e^- and •O_2^- are the main active species involved in the photocatalytic reaction. What is more, the EPR spin-trap experiment is conducted to verify the generation active species which are trapped by TMPO (or DMPO) to form transient radical intermediates (TMPO-e^-, DMPO-•OH and DMPO-•O_2^-) under irradiation. As displayed in Fig. 7b, in the **ECUT-AQ** photocatalytic system, no obvious DMPO-•OH characteristic signal is observed either in the dark or under irradiation, which is due to the HOMO of **ECUT-AQ** (+1.17 V) is much higher than the potential position of OH^-/•OH (+1.99 V) and H_2O/•OH (+2.34 V) couples, resulting in impoverished driving force to convert OH^- or H_2O to •OH. However, the characteristic sextet peaks of DMPO-•O_2^- and triplet semaphore with equal peak height of TMPO-e^- adducts are detected under irradiation (Fig. 7c and d), suggesting that both •O_2^- radical and e^- are efficiently generated during photocatalysis. Therefore, it is concluded that e^-, h^+ and •O_2^- are the main active species involved in the photoreduction of uranium, and directly dominate the activity of photocatalytic reduction of uranium.

In conjunction with the above discussion, the possible photoreduction mechanism of U(VI) on **ECUT-AQ** is elaborated and depicted in Fig. 8. Under irradiation ($\lambda \geq 400$ nm), the **ECUT-AQ** with D-A structure is excited by photons, resulting in a large number of e^-/h^+ pairs. Then, driven by a strong built-in electric field, the e^-/h^+ pairs are effectively separated. Next, the electrons are rapidly transferred from the HOMO to the LUMO through efficient charge transfer channels (reversible redox process of AQ in strong acid solution), while the holes remain on the HOMO. After that, a small fraction of the activated electrons straightly reduces the surface UO_2^{2+} to UO_2. At this time, most of the remaining photo-generated electrons interact violently with oxygen to yield more reductive •O_2^- radicals, which acts as an active specie to further reduce the adsorbed UO_2^{2+} to UO_2. Synchronously, the holes rapidly oxidize AA
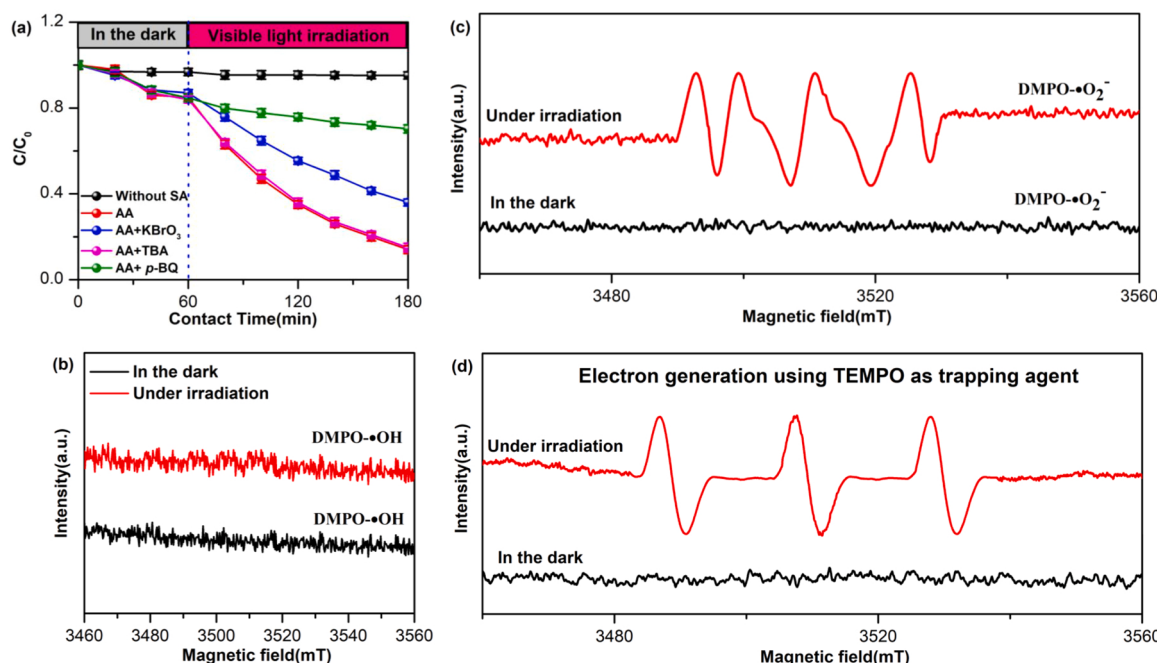
Fig. 7. (a) Removal of U(VI) by **ECUT-AQ** with e^- ($KBrO_3$), h^+ (AA), •OH (TBA) and •O_2^- (*p*-BQ) radical scavenger under visible light irradiation; (b) ESR spectra of DMPO-•OH and (c) DMPO-•O_2^- for **ECUT-AQ** in the dark and under irradiation; (d) electron generation using TEMPO as trapping agent in the dark and under irradiation. Typically, TEMPO as the electron capture agent can be reduced to produce an ESR-silent product TEMPOH, which is usually employed to monitor the photogenerated electrons.
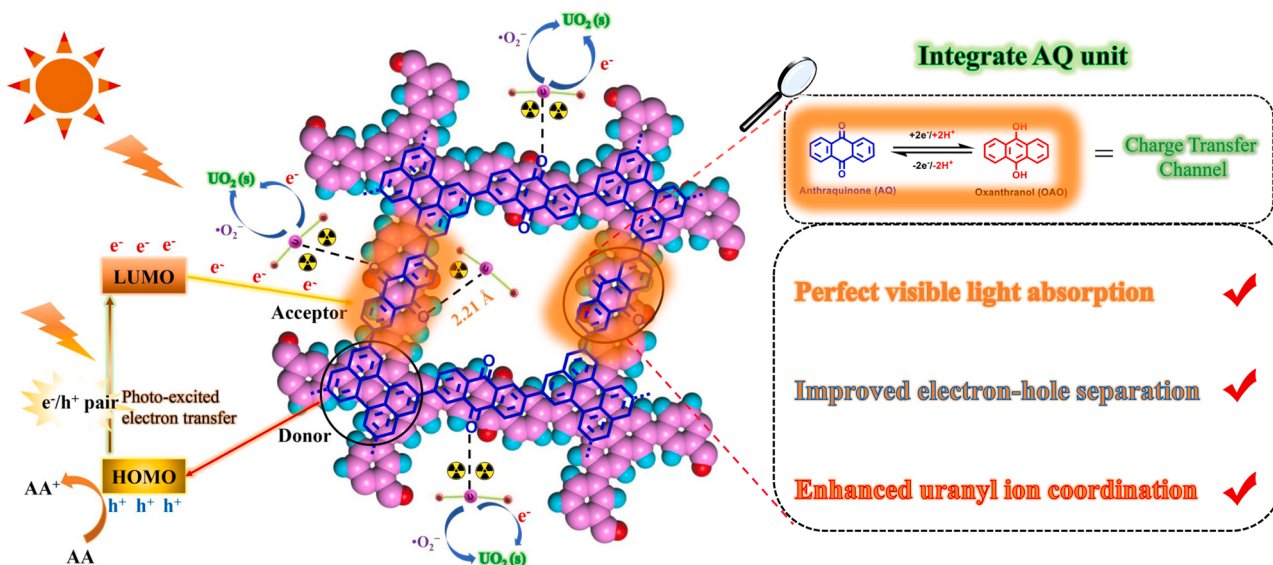
Fig. 8. The proposed photocatalytic U(VI) reduction mechanism of the **ECUT-AQ**.

to AA$^+$ (dehydroascorbic acid), and the whole photocatalytic process is completed. As a result, the distinctive charge transfer route via AQ-based reversible redox reaction can effectively speed up electron migration along the polymer backbone and inhibit the bulk recombination of electrons and holes, thereby significantly enhancing photocatalytic activity of **ECUT-AQ**.

4. Conclusions

In summary, we have purposefully synthesized D−A type redox-active conjugated microporous polymer (**ECUT-AQ**) and innovatively used it for visible-light-driven photocatalytic reduction U(VI) in strong acid solution. Interestingly, experiments combined with theoretical calculations have elucidated that the redox-active AQ unit plays a decisive role in the photocatalytic reduction of uranium. Since AQ is an electron-deficient group containing two carbonyls, it can not only improve the binding affinity for uranyl ions, but also facilitate the intramolecular charge transfer process, resulting in better visible light absorption and facilitated electron-hole pair separation. In addition, AQ possesses excellent redox activity, acting as an electron delocalization channel to rapidly transfer electrons and inhibit the recombination of photogenerated carriers. As a result, the **ECUT-AQ** obtains 86% photoreduction U(VI) efficiency within 120 min irradiation and corresponding reduction rate constant at 293.15 K is 0.015 min^{-1} (pH=1). In short, the present finding provides a general strategy for efficiently constructing heterogeneous photocatalysts with high photocatalytic performance for U(VI) reduction in harsh environment, bringing the photoreduction U(VI) technology one solid step closer to industrialization.

CRediT authorship contribution statement

Fengtao Yu: Investigation, Methodology, Validation, Funding acquisition, Project administration, Writing – original draft. **Zhiqiang Zhu**: Investigation, Formal analysis, Validation. **Chuangye Li**: Methodology, Investigation. **Wanru Li**: Data curation. **Renping Liang**: Investigation, Methodology. **Shanshan Yu**: Investigation, Validation. **Zhenzhen Xu**: Software, Data curation. **Fangru Song**: Funding acquisition, Investigation. **Qiang Ren**: Writing – review & editing. **Zhibin Zhang**: Conceptualization, Writing – review & editing, Supervision, Project administration, Resources.

Declaration of Competing Interest

The authors declare no competing fnancial interest.

Acknowledgements

Appendix A. Supporting information

Supplementary data associated with this article can be found in the online version at doi:10.1016/j.apcatb.2022.121467.

References

[1] A. Adamantiades, I. Kessides, Nuclear power for sustainable development: current status and future prospects, Energy Policy 37 (2009) 5149–5166.
[2] Z.M. Dong, Z.B. Zhang, Z.F. Li, Y.C. Wang, F.T. Yu, Z.P. Cheng, Y. Dai, X.H. Cao, Y.Q. Wang, Y.H. Liu, X.L. Fan, Double-shelled hollow nanosphere assembled by TiO$_2$@surface sulfate functionalized CdS for boosting photocatalysis reduction of U(VI) under seawater conditions, Chem. Eng. J. 431 (2022) 133256–133268.
[3] P.G. Mouser, A.L. N'Guessan, H. Elifantz, D.E. Holmes, K.H. Williams, M.J. Wilkins, P.E. Long, D.R. Lovley, Influence of heterogeneous ammonium availability on bacterial community structure and the expression of nitrogen fixation and ammonium transporter genes during in situ bioremediation of uranium-contaminated groundwater, Environ. Sci. Technol. 43 (2009) 4386–4392.
[4] Z.M. Dong, Z. bin Zhang, Z.F. Li, Y. Feng, W.J. Dong, T. Wang, Z.P. Cheng, Y.Q. Wang, Y. Dai, X.H. Cao, Y.H. Liu, Y.H. Liu, 3D structure aerogels constructed by reduced graphene oxide and hollow TiO$_2$ spheres for efficient visible-light-driven photoreduction of U(VI) in air-equilibrated wastewater, Environ. Science: Nano 8 (2021) 2372–2385.
[5] S. Chu, A. Majumdar, Opportunities and challenges for a sustainable energy future, Nature 488 (2012) 294–303.
[6] Y. Yuan, Y.J. Yang, X.J. Ma, Q.H. Meng, L.L. Wang, S. Zhao, G.S. Zhu, Molecularly imprinted porous aromatic frameworks and their composite components for selective extraction of uranium ions, Adv. Mater. 30 (2018) 1706507–1706513.
[7] Z.L. Bai, Y.L. Wang, Y.X. Li, W. Liu, L.H. Chen, D.P. Sheng, D.W. Juan, Z.F. Chai, T.E. Albrecht-Schmitt, S.A. Wang, First cationic uranyl–organic framework with anion-exchange capabilities, Inorg. Chem. 55 (2016) 6358–6360.
[8] W.S. Luo, S.D. Kelly, K.M. Kemner, D. Watson, J.Z. Zhou, P.M. Jardine, B.H. Gu, Sequestering uranium and technetium through co-precipitation with aluminum in a contaminated acidic environment, Environ. Sci. Technol. 43 (2009) 7516–7522.

[9] X. Zhang, L. Yuan, Z. Chai, W. Shi, Towards understanding the correlation between UO_2^{2+} extraction and substitute groups in 2,9-diamide-1,10-phenanthroline, Sci. China Chem. 61 (2018) 1285–1292.

[10] Y. Guo, Y. Guo, X. Wang, P. Li, L. Kong, G. Wang, X. Li, Y. Liu, Enhanced photocatalytic reduction activity of uranium(vi) from aqueous solution using the Fe_2O_3-graphene oxide nanocomposite, Dalton Trans. 46 (2017) 14762–14770.

[11] Z.M. Dong, Z. bin Zhang, T. Wang, D.L. Zeng, Z.P. Cheng, Y.C. Wang, X.H. Cao, Y. Q. Wang, Y.H. Liu, X.L. Fan, Ingenious design of ternary hollow nanosphere with shell hierarchical tandem heterojunctions toward optimized visible-light photocatalytic reduction of U(VI), Sep. Purif. Technol. 286 (2022) 120418–120430.

[12] P.L. Liang, L.Y. Yuan, K. Du, L. Wang, Z.J. Li, H. Deng, X.C. Wang, S.Z. Luo, W. Q. Shi, Photocatalytic reduction of uranium (VI) under visible light with 2D/1D Ti_3C_2/CdS, Chem. Eng. J. 420 (2021) 129831–129840.

[13] C. Liu, Z.M. Dong, C.H. Yu, J.Y. Gong, Y.Q. Wang, Z.B. Zhang, Y.H. Liu, Study on photocatalytic performance of hexagonal SnS_2/g-C_3N_4 nanosheets and its application to reduce U(VI) in sunlight, Appl. Surf. Sci. 537 (2021) 147754–147764.

[14] X.L. Tong, S. Wang, J. Zuo, Y.C. Ge, Q. Gao, S.J. Liu, J.H. Ding, F. Liu, J.Q. Luo, J. B. Xiong, Two 2D uranyl coordination complexes showing effective photocatalytic degradation of Rhodamine B and mechanism study, Chin. Chem. Lett. 32 (2021) 604–608.

[15] D. Kong, X.Y. Han, J.J. Xie, Q.S. Ruan, C.D. Windle, S. Gadipelli, K. Shen, Z.M. Bai, Z.X. Guo, J.W. Tang, Tunable covalent triazine-based frameworks (CTF-0) for visible-light-driven hydrogen and oxygen generation from water splitting, ACS Catal. 9 (2019) 7697–7707.

[16] S.Y. Li, X.Y. Yang, Z.P. Cui, Y. Xu, Z.W. Niu, P. Li, D.Q. Pan, W.S. Wu, Efficient photoreduction strategy for uranium immobilization based on graphite carbon nitride/perovskite oxide heterojunction nanocomposites, Appl. Catal. B Environ. 298 (2021) 120625–120633.

[17] F.T. Yu, Z.Q. Zhu, Z.Z. Xu, J.B. Xiong, Q.W. Fan, X.F. Feng, Y. Tao, J.L. Hua, F. Luo, Heteroatom engineering of polymeric carbon nitride heterojunctions for boosting photocatalytic reduction of hexavalent uranium, Mol. Syst. Des. Eng. 5 (2020) 882–889.

[18] F.T. Yu, Z.Q. Wang, S.C. Zhang, H.N. Ye, K.Y. Kong, X.Q. Gong, J.L. Hua, H. Tian, Molecular engineering of Donor-Acceptor conjugated polymer/g-C_3N_4 heterostructures for significantly enhanced hydrogen evolution under visible-light irradiation, Adv. Funct. Mater. 28 (2018) 1804512–1804524.

[19] L. Chen, B. Chen, J.Y. Kang, Z.J. Yan, Y.D. Jin, H.J. Yan, S.Y. Chen, C.Q. Xia, The synthesis of a novel conjugated microporous polymer and application on photocatalytic removal of uranium (VI) from wastewater under visible light, Chem. Eng. J. 431 (2022) 133222–133230.

[20] J. Xu, S.H. An, X.Y. Song, Y.J. Cao, N. Wang, X. Qiu, Y. Zhang, J.W. Chen, X. L. Duan, J.H. Huang, W. Li, Y.G. Wang, Towards high performance Li-S batteries via sulfonate-rich COF-modified separator, Adv. Mater. 33 (2021) 2105178–2105187.

[21] W.R. Cui, C.R. Zhang, R.P. Liang, J.D. Qiu, Covalent organic framework hydrogels for synergistic seawater desalination and uranium extraction, J. Mater. Chem. A 9 (2021) 25611–25620.

[22] W.R. Cui, F.F. Li, R.H. Xu, C.R. Zhang, X.R. Chen, R.H. Yan, R.P. Liang, J.D. Qiu, Regenerable covalent organic frameworks for photo-enhanced uranium adsorption from seawater, Angew. Chem. Int. Ed. 59 (2020) 17684–17690.

[23] Y.C. Xu, H.S. Zhang, Q. Liu, J.Y. Liu, R.R. Chen, J. Yu, J.H. Zhu, R.M. Li, J. Wang, Surface hybridization of π-conjugate structure cyclized polyacrylonitrile and radial microsphere shaped TiO_2 for reducing U(VI) to U(IV), J. Hazard. Mater. 416 (2021) 125812–125820.

[24] X.H. Jiang, Q.J. Xing, X.B. Luo, F. Li, J.P. Zou, S.S. Liu, X. Li, X.K. Wang, Simultaneous photoreduction of Uranium (VI) and photooxidation of Arsenic (III) in aqueous solution over g-C_3N_4/TiO_2 heterostructured catalysts under simulated sunlight irradiation, Appl. Catal. B Environ. 228 (2018) 29–38.

[25] E. Selli, V. Eliet, M.R. Spini, G. Bidoglio, Effects of humic acids on the photoinduced reduction of U(VI) in the presence of semiconducting TiO_2 particles, Environ. Sci. Technol. 34 (2000) 3742–3748.

[26] Z.F. Li, Z.B. Zhang, Z.M. Dong, F.T. Yu, M.Y. Ma, Y.C. Wang, Y.Q. Wang, Y.H. Liu, J. Liu, X.H. Cao, Y.H. Liu, Solar Light-Responsive CdS/UiO-66-NH2 for ultrafast uranium reduction from uranium-containing mine wastewater without external sacrificial agents, Sep. Purif. Technol. 283 (2020) 120195–120203.

[27] H. Deng, Z.J. Li, L. Wang, L.Y. Yuan, J.H. Lan, Z.Y. Chang, Z.F. Chai, W.Q. Shi, Nanolayered Ti_3C_2 and $SrTiO_3$ composites for photocatalytic reduction and removal of uranium (VI), ACS Appl. Nano Mater. 2 (2019) 2283–2294.

[28] Z.W. Zhang, J. Jia, Y.F. Zhi, S. Ma, X.M. Liu, Porous organic polymers for light-driven organic transformations, Chem. Soc. Rev. 51 (2022) 2444–2490.

[29] Z.P. Li, J.A. Wang, S. Ma, Z.W. Zhang, Y.F. Zhi, F.C. Zhang, H. Xia, G. Henkelman, X.M. Liu, 2D covalent organic frameworks for photosynthesis of α-trifluoromethylated ketones from aromatic alkenes, Appl. Catal. B 310 (2022), 121335.

[30] S. Ma, Z.P. Li, J. Jia, Z.W. Zhang, H. Xia, H. Li, X. Chen, Y.H. Xu, X.M. Liu, Amide-linked covalent organic frameworks as efficient heterogeneous photocatalysts in water, Chin. J. Catal. 42 (2021) 2010–2019.

[31] F.T. Yu, Z.Q. Zhu, S.P. Wang, Y.K. Peng, Z.Z. Xu, Y. Tao, J.B. Xiong, Q.W. Fan, F. Luo, Tunable perylene-based donor-acceptor conjugated microporous polymer to significantly enhance photocatalytic uranium extraction from seawater, Chem. Eng. J. 412 (2021) 127558–127569.

[32] F.T. Yu, Z.Q. Zhu, J.Y. Wang, J.Y. Wang, Z.Z. Xu, F.R. Song, Z.M. Dong, Z.B. Zhang, Novel donor-acceptor-acceptor ternary conjugated microporous polymers with boosting forward charge separation and suppressing backward charge recombination for photocatalytic reduction of uranium (VI), Appl. Catal. B Environ. 301 (2022) 120819–120829.

[33] M.Y. Xu, X.L. Han, T. Wang, S.H. Li, D.B. Hua, Conjugated microporous polymers bearing phosphonate ligands as an efficient sorbent for potential uranium extraction from high-level liquid wastes, J. Mater. Chem. A 6 (2018) 13894–13900.

[34] P. Li, Y. Wang, J.J. Wang, L. Dong, W.T. Zhang, Z.H. Lu, J.J. Liang, D.Q. Pan, Q. H. Fan, Carboxyl groups on g-C_3N_4 for boosting the photocatalytic U(VI) reduction in the presence of carbonates, Chem. Eng. J. 414 (2021) 128810–128818.

[35] Z.R. Dai, Y. Zhen, Y.S. Sun, L. Li, D.X. Ding, $ZnFe_2O_4$/g-C_3N_4 S-scheme photocatalyst with enhanced adsorption and photocatalytic activity for uranium (VI) removal, Chem. Eng. J. 415 (2021) 129002–129011.

[36] L. Ke, P. Li, X. Wu, S. Jiang, M. Luo, Y. Liu, Z. Le, C. Sun, S. Song, Graphene-like sulfur-doped g-C3N4 for photocatalytic reduction elimination of UO22+ under visible Light, Appl. Catal. B Environ. 205 (2017) 319–326.

[37] W.Z. Zhang, L. Li, Y.H. Gao, D. Zhang, Graphitic carbon nitride-based materials for photocatalytic reduction of U(vi), N. J. Chem. 44 (2020) 19961–19976.

[38] E. Selli, V. Eliet, M.R. Spini, G. Bidoglio, Effects of humic acids on the photoinduced reduction of U(VI) in the presence of semiconducting TiO_2 particles, Environ. Sci. Technol. 34 (2000) 3742–3748.

[39] F.T. Yu, F.R. Song, R.Z. Wang, M. Xu, F. Luo, Sulfonated perylene-based conjugated microporous polymer as a high-performance adsorbent for photo-enhanced uranium extraction from seawater, Polym. Chem. 12 (2021) 867–875.

[40] X. Ma, S.Y. Wang, L.F. Qin, J. Liu, B. Li, Y.N. Hu, H.F. Cheng, Z-scheme g-C3N4-AQ-MoO3 photocatalyst with unique electron transfer channel and large reduction area for enhanced sunlight photocatalytic hydrogen production, Appl. Catal. B Environ. 288 (2021) 120025–120038.

[41] X. Ma, S.Y. Li, Z.H. Qu, M. Zhang, J. Qiao, X. Cui, C.Q. Wang, J. Wang, Y. Song, A highly active Z-scheme NiGa2O4/anthraquinone/MoO3 photocatalyst via charge transfer for sunlight photocatalytic simultaneous conversions of nitrite and sulfite, J. Ind. Eng. Chem. 78 (2019) 303–314.

[42] L.F. Zhong, Z.S. Fang, C.H. Shu, C.S. Mo, X.C. Chen, D.S. Yu, Redox donor-acceptor conjugated microporous polymers as ultralong-lived organic anodes for rechargeable air batteries, Angew. Chem. Int. Ed. 60 (2021) 10164–10171.

[43] J.C. González, D.A. Vosburg, S.E. Mora-Rodriguez, M.A. Vázquez, L.G. Zepeda, C. V. Gómez, S. Lagunas-Rivera, Anthraquinones: versatile organic photocatalysts, ChemCatChem. 12 (2020) 3811–3827.

[44] Y.F. Zhi, S. Ma, H. Xia, Y.M. Zhang, Z. Shi, Y. Mu, X.M. Liu, Construction of donor-acceptor type conjugated microporous polymers: a fascinating strategy for the development of efficient heterogeneous photocatalysts in organic synthesis, Appl. Catal. B Environ. 244 (2019) 36–44.

[45] H. Kim, Y. Choi, S. Hu, W.Y. Choi, J.H. Kim, Photocatalytic hydrogen peroxide production by anthraquinone-augmented polymeric carbon nitride, Appl. Catal. B Environ. 244 (2019) 36–44.

[46] T. Yanai, D. Tew, N. Handy, A new hybrid exchange–correlation functional using the coulomb-attenuating method (CAM-B3LYP), Chem. Phys. Lett. 393 (2004) 51–57.

[47] C. Less, W. Yang, R.G. Parr, Development of the Colle-Salvetti correlation-energy formula into a functional of the electron density, Phys. Rev. B 37 (1988) 785–789.

[48] J. Yang, J.F. Jing, Y.F. Zhu, A full-spectrum porphyrin–fullerene D–A supramolecular photocatalyst with giant built-in electric field for efficient hydrogen production, Adv. Mater. 33 (2021) 2101026–2101033.

[49] F. Chen, H.W. Huang, L. Guo, Y.H. Zhang, T.Y. Ma, The role of polarization in photocatalysis, Angew. Chem. Int. Ed. 58 (2019) 10061–10073.

[50] J. Li, L.J. Cai, J. Shang, Y. Yu, L.Z. Zhang, Giant enhancement of internal electric field boosting bulk charge separation for photocatalysis, Adv. Mater. 28 (2016) 4059–4064.

[51] X.M. Gao, K.L. Gao, W. Zhu, C.H. Liang, Q.G. Li, F. Fu, Y.F. Zhu, Accurate guided alternating atomic layer enhance internal electric field to steering photogenerated charge separation for enhance photocatalytic activity, Appl. Catal. B 298 (2021) 120536–120547.